

Femtosecond Synchronization of Optical Clocks Off of a Flying Quadcopter

Hugo Bergeron⁺, Laura C. Sinclair^{*,+}, William C. Swann, Isaac Khader, Kevin C. Cossel, Michael Cermak, Jean-Daniel Deschênes^{*}, and Nathan R. Newbury

¹*National Institute of Standards and Technology, 325 Broadway, Boulder, Colorado 80305*

²*Université Laval, 2325 Rue de l'Université, Québec, QC, G1V 0A6, Canada*

⁺ These authors contributed equally to this work.

**laura.sinclair@nist.gov; octosigconsulting@gmail.com; nathan.newbury@nist.gov*

Work of the U.S. Government and not subject to copyright.

Optical clock networks promise advances in global navigation, time distribution, coherent sensing, relativity experiments, dark matter searches and other areas^{1–12}. Such networks will need to compare and synchronize clocks over free-space optical links. Optical two-way time-frequency transfer (O-TWTFT) has synchronized clocks to 10^{-19} in frequency and <1 fs in time across turbulent free-space links^{16–19}, but only between stationary terminals where reciprocity in time-of-flight across the single-mode link underwrites the performance. Any motion leads to breakdown in this time-of-flight reciprocity and in O-TWTFT performance. Here, we show the inclusion of velocity-dependent effects into comb-based O-TWTFT can allow for penalty-free operation. We synchronize clocks connected via a quadcopter-mounted retroreflector or swept delay line over turbulent air paths at speeds up to 24 m/s. The synchronized clocks agree to $\sim 10^{-18}$ in frequency, despite 10^{-7} Doppler shifts, and to <1 fs in time deviation, despite 50-ps breakdown in time-of-flight reciprocity.

The use of two-way or round-trip timing signals to cancel time-of-flight variations underpins both rf/microwave time-frequency transfer via free-space^{17,18} and optical time-frequency transfer via fiber optics^{7–10,19–23}. However, the optical system used for fiber-optic links cannot be applied to free-space links because of the following challenges. First, the received free-space signals will incur fades and strong variations due to turbulence. Second, the signals will be weak as mid-span amplification is not an option. Third, the absolute distance between sites is not fixed by the physical

fiber. Finally, and most importantly, the two end sites can move, leading to a complete breakdown in the assumption of reciprocity. Consider even a modest terrestrial velocity of 30 m/s between clock sites. The non-reciprocal Doppler shift of 10^{-7} must be suppressed by $\times 10^{11}$ to synchronize clocks to 10^{-18} in frequency. At this same velocity, the non-reciprocal time-of-flight of 3 ps (due to the finite speed-of-flight) must be suppressed by $\times 10^4$ to synchronize clocks to below 1 fs in time. Moreover, the two-way time-frequency transfer system must suppress these effects despite strong variations in velocity with acceleration and despite recurrent turbulence-induced loss of signal. Here, we show comb-based O-TWTFT can address these challenges by implementation of new underlying synchronization equations that account for relativistic and systematic timing effects, exploitation of all available information from the O-TWTFT system, and significant hardware modifications, culminating in residual noise below the best state-of-the-art optical clocks and oscillators.

Although the overall comb-based O-TWTFT is complex, it can be formally simplified to two-way time-transfer wherein one signal departs site A at time T_{AA} , as recorded at site A, and arrives at site B at time $T_{AB} = T_{AA} + T_{A \rightarrow B} - \Delta t_{AB}$, as recorded at site B, where Δt_{AB} is the time offset between sites and $T_{A \rightarrow B}$ is the time-of-flight from A to B. A second signal departs site B at time T_{BB} and arrives at site A at time $T_{BA} = T_{BB} + T_{B \rightarrow A} + \Delta t_{AB}$ where $T_{B \rightarrow A}$ is the time-of-flight from B to A. Combined, these four timestamps yield the clock time offset as

$$\Delta t_{AB} = \frac{1}{2} [T_{AA} - T_{AB} - T_{BB} + T_{BA}] + \frac{1}{2} [T_{A \rightarrow B} - T_{B \rightarrow A}] + \Delta T_{cal} \quad (1)$$

where ΔT_{cal} is an overall transceiver calibration. The middle term is the breakdown in time-of-flight reciprocity which is assumed zero for links between fixed terminals. Note that for the O-TWTFT system, the four effective timestamps $\{T_{AA}, T_{AB}, T_{BB}, T_{BA}\}$ are actually derived from

multiple measurements involving three frequency combs and a parallel optical communication channel. (See Methods and Ref. 24.)

Now consider the case realized here experimentally of two clocks connected via a mirror moving at closing velocity $V/2$ away from the clocks (i.e. perpendicular to a line connecting the two clock sites). The mirror is at a distance $L_A(t)$ from site A and $L_B(t)$ from site B. This scenario mimics time-transfer via a moving, intermediate clock site. The problem can be generalized to the alternate scenario of a stationary clock A and moving clock B with inclusion of the time dilation effect. The initial consequence of motion is the breakdown in reciprocity

$$T_{A \rightarrow B} - T_{B \rightarrow A} = (V/c)(T_{AB} - T_{BA} + \Delta t_{AB}) + (V/c^2)(L_A - L_B), \quad (2)$$

to first order in V/c , where c is the speed of light. The first term results from the asynchronous sampling and the second from the finite speed of light, which can be derived from geometric considerations or more formally via Lorentz transformations²⁵. At a modest $V=30$ m/s, 4-km link, and 0.5-ms asynchronous sampling ($T_{AB} \neq T_{BA}$), the two terms in (2) yield a non-reciprocal time-of-flight of 50 ps and 1.3 ps, respectively. This would be misinterpreted as a clock offset unless this non-zero non-reciprocity, (2), were included in the time offset calculation, (1). We include the non-reciprocity to < 100 as precision by using the available O-TWTFT data to calculate the asynchronous sampling to sub-femtosecond precision and the speed to 250 $\mu\text{m/s}$ precision. The speed is found from the rate-of-change of the measured time-of-flight over three roughly continuous measurements requiring ~ 1.5 ms across a turbulent link.

The additional effects of motion are far more complicated and discussed in-depth in Ref. 24. Both relate to the Doppler shifts, which are large (10^{-7} even at $V=30$ m/s) and changing as V is not constant. First, the transceiver calibration term, ΔT_{cal} , is velocity-dependent because of the distributed nature of the transceivers. Therefore, $\Delta T_{\text{cal}} \rightarrow \Delta T_{\text{cal}} + (V/c)\Delta T_{\text{cal}}^V$, where the

independent calibration of ΔT_{cal} and ΔT_{cal}^V is system dependent²⁴. Second, system dispersion will couple Doppler shifts to systematic picosecond-level timing errors in T_{AB} and T_{BA} . In general, one expects a systematic timing error roughly equal to the product of the Doppler shift and the second-order dispersion. However, the use of linear optical sampling, which is critical to measuring the comb pulse arrivals with sub-femtosecond precision, has the unfortunate ancillary effect of amplifying any delay-Doppler coupling due to differential dispersion by $f_r/\Delta f_r \sim 10^5$. Critically, we suppress this systematic to below 100 as by a hardware design that minimizes dispersion and by a real-time algorithm that extracts arrival times from the cross-ambiguity function (see Methods).

Figure 1 shows the basic setup. Sites A and B each comprise a O-TWTFT transceiver and comb-based optical timescale, which is referenced to a local cavity-stabilized laser. The link is folded to enable verification by a direct time comparison between sites at a common reference plane^{14–16}. Because a fully “flyable” optical clock/oscillator is currently unavailable, we instead change the distance between sites by a quadcopter-mounted retroreflector or a rapidly swept delay line. In either case, the link also includes a 2- or 4-km free-space turbulent air path. The closing velocity is physically limited to ± 24 m/s (± 86 km/hr) but the approach scales to higher velocities.

The system uses a layered approach: TWTFT with a modulated communication channel for picosecond-level time transfer²⁶ followed by TWTFT with coherent frequency comb pulses for femtosecond-level time transfer^{13–15}. This frequency-comb TWTFT uses linear-optical sampling (LOS) to achieve femtosecond precision (with a 5-nanosecond ambiguity given by the ~ 200 -MHz comb repetition rate). LOS requires the repetition rate of the two pulse trains transmitted across the link differ by $\Delta f_r \sim 2$ kHz¹⁴, which leads to inclusion of a third “transfer” comb at the master site. The timing data from the communication channel and frequency-comb transfer are input into new synchronization algorithms (see Methods and Ref. 24) that, unlike Refs. 14–16, resolve the

5-ns ambiguity on the comb pulse-by-pulse and incorporate the multiple picosecond-level motion-induced effects described above. These algorithms are implemented in a field-programmable gate array and digital signal processing platform to generate an estimate of Δt_{AB} in real time at the 2-kHz measurement rate. Under strong turbulence, signal fades block the exchange of comb pulses and the communication link, but these fades are usually of short duration. Therefore, a Kalman filter allows continuous operation through such dropouts¹⁵. The filter's output adjusts the phase of the clock at site B to synchronize the clocks at 10-100 Hz feedback bandwidth¹⁵.

Figure 2 shows time synchronization with the swept delay line operated at closing velocities from 0 m/s to ± 24 m/s and including 4 km of turbulent air. The time-of-flight, closing velocity, and calculated time offset are all returned from the O-TWTFT signals. In parallel, the clocks' time offset is measured by the out-of-loop verification. When actively synchronized, the clock times agree with a standard deviation of 1.1 fs at the full 2.2 kHz update rate. During brief signal fades due to atmospheric turbulence, the clocks' times walk off randomly (cyan trace of Figure 2(b)) but are resynchronized when the signal is re-acquired.

Synchronization to a quadcopter-mounted retroreflector is shown in Supplementary Video 1 and Figure 3. The quadcopter obtained a maximum 500-meter optical pathlength change and a 20 m/s (quadcopter-limited) maximum speed. Again, we see femtosecond-level synchronization with no evidence of speed-dependent bias. These data do show much longer fades due to the additional challenge of tracking the moving quadcopter²⁷.

Figure 4 shows the time and modified Allan deviations. For these data, the swept delay line was operated for > 20 minutes at ± 24 m/s with free-space links of 0, 2, and 4 km. The resulting time deviations, calculated from the out-of-loop verification, all remain below 1 fs for averaging times from 0.1 seconds (the inverse of the synchronization bandwidth) to 100 seconds and are essentially

unchanged from a static 0-km shorted measurement. For the quadcopter data, the time deviation remains at ~ 1 fs at all averaging times, elevated slightly above the delay-line data due to longer fades and calibration uncertainties associated with the tracking terminal. The relative fractional frequency instability (modified Allan deviation) for the swept-delay line data is below 10^{-15} at a 1-second averaging time and 10^{-18} at a 200-second averaging time at all closing velocities. For the quadcopter data, it is 2×10^{-15} at a 1-second averaging time and 2×10^{-17} at a 100-second averaging time.

Further analysis shows our approach mitigates all velocity-dependent bias to within a two-sigma confidence of 330 as (see Ref. 24). However, future high speed airborne or satellite-based platforms will operate at significantly higher speeds and therefore will require inclusion of additional acceleration and even $(V/c)^2$ terms as well as hardware/algorithm modification to treat Doppler shifts that exceed the comb repetition rate of 200 MHz. (Non-reciprocity due to “point-ahead” effects should be negligible^{28,29}.) Nevertheless, the current results indicate no fundamental limitations to O-TWTFT, allowing for future optical clock networks with sub-femtosecond synchronization and 10^{-18} frequency syntonization to support multiple time-frequency based precision measurements.

Methods

Each site A and B comprise their own comb-based optical timescale and O-TWTFT transceiver. For example, to define a timescale at the master site, comb A is phase-locked to a local optical oscillator (cavity-stabilized laser at ~ 195 THz) to generate pulses labelled with integer n_A and separated by f_r^{-1} . These arrive at the local defined reference plane at times $t_A = n_A f_r^{-1} + \tau_A$. In this formulation, f_r is the nominal defined repetition frequency and τ_A encompasses not only the fixed time offsets to the reference plane but any slow variations from the phase drift, or equivalently integrated frequency error, in the local comb. At the remote site, comb B is phase-locked to another optical oscillator (or possibly a quartz rf oscillator), generating pulses labelled with integer n_B and nominally separated also by f_r^{-1} ; these arrive at the defined reference plane at times $t_B = n_B f_r^{-1} + \tau_B$, where again τ_B is the slowly varying clock offset and the nominal f_r ~ 200 MHz is identical to site A. For verification purposes, we use a common reference plane at which the time offset is $\Delta t_{AB} \equiv t_A - t_B$.

The linear optical sampling (LOS) detection used in comb-based O-TWTFT requires the pulse trains of the two combs transmitted across the link have repetition rates differing by $\Delta f_r \sim 2$ kHz¹⁴, but the two combs that generate the timescale have identical repetition rates. Therefore, we introduce a third, transfer comb X at the master site with repetition rate $f_r + \Delta f_r$ and time offset τ_X , also phase-locked to the master optical oscillator.

The overall system follows Ref. 14 closely except that the overall dispersion in the transceivers was reduced thirty-fold, transceiver calibration was performed by a custom, integrated optical time domain reflectometer (OTDR), an rf re-design was required to reduce multipath reflections due to

impedance mismatches, the rf group delay vs frequency curves had to be carefully measured and digitally cancelled prior to interferogram detection and the new algorithms required more extensive digital signal processing hardware.

The three measured heterodyne signals between the master, transfer, and remote combs consist of a series of consecutive interferograms, i.e short heterodyne pulse envelopes, as the pulses cross each other at a rate Δf_r . If we label each interferogram by an integer p with appropriate subscripts, the three signals are:

$$\begin{aligned} I_{AX}(t) &\approx \sum_{p_{AX}} I_{AX}(t - t_{AX}[p_{AX}]) : \text{Master} \rightarrow \text{Transfer} , \\ I_{BX}(t) &\approx \sum_{p_{BX}} I_{BX}^V(t - t_{BX}[p_{BX}]) : \text{Remote} \rightarrow \text{Transfer} \\ I_{XB}(t) &\approx \sum_{p_{XB}} I_{XB}^V(t - t_{XB}[p_{XB}]) : \text{Transfer} \rightarrow \text{Remote} \end{aligned}$$

where $I_{BX}^V(t)$, $I_{XB}^V(t)$, and $I_{AX}(t)$ are the interferogram pulse shapes as seen in Fig. 6 of Ref. 24, and t is some oracle timescale. The first interferogram, I_{AX} , is generated from the local heterodyne mixing of the master and transfer comb at the master site. The middle interferogram, I_{BX} , is the heterodyne signal between the transmitted remote comb pulses and the transfer comb at the master site. The third interferogram, I_{XB} , is the heterodyne signal between the transmitted transfer comb and the remote comb at the remote site. We are ultimately interested in the times $t_{AX}[p_{AX}]$, $t_{BX}[p_{BX}]$, and $t_{XB}[p_{XB}]$ that define the centers of the successive interferograms since we will combine these timing data with the communication-based two-way time-frequency transfer to evaluate Δt_{AB} .

Unfortunately, the interferograms' waveform depends on the Doppler shift of the incoming light (and therefore on velocity as indicated by the superscript) and this, coupled with the relative chirp between the comb pulses, can cause an apparent timing shift if the center of the interferogram is evaluated by correlation with a matched filter as in Ref. 14. To avoid this inherent delay-Doppler

coupling bias, we instead conduct a real-time, two-dimensional search using the expected cross-ambiguity function³⁰. Assuming successful suppression of this velocity-induced bias and following similar analysis as in Ref. 14, the three times are

$$\begin{aligned} t_{\text{pAX}} &= \Delta f_r^{-1} \{ p_{\text{AX}} - [f_r + \Delta f_r] \tau_{\text{X}} + f_r \tau_{\text{A}} \} \\ t_{\text{pBX}} &= \Delta f_r^{-1} \{ p_{\text{BX}} - f_r T_{\text{B} \rightarrow \text{A}}(t_{\text{pBX}}) + f_r \tau_{\text{B}} - [f_r + \Delta f_r] \tau_{\text{X}} \} \\ t_{\text{pXB}} &= \Delta f_r^{-1} \{ p_{\text{XB}} + [f_r + \Delta f_r] T_{\text{A} \rightarrow \text{B}}(t_{\text{pXB}}) + f_r \tau_{\text{B}} - [f_r + \Delta f_r] \tau_{\text{X}} \} \end{aligned} \quad (3)$$

as measured with respect to the oracle timescale t . In the system however, the timestamps are instead measured against the local timescale at site A or B. Therefore, we use the relationships $t_{\text{pAX}} = f_r^{-1} k_{\text{pAX}} - \tau_{\text{A}}$, $t_{\text{pBX}} = f_r^{-1} k_{\text{pBX}} - \tau_{\text{A}}$, and $t_{\text{pXB}} = f_r^{-1} k_{\text{pXB}} - \tau_{\text{B}}$, because $\tau_{\text{A(B)}}$ are the time offsets of the site A(B) timescale from oracle time and $f_r^{-1} k$ is the definition of a local time with k representing the not-necessarily integer ADC sample number. Note that the function $T_{\text{A} \rightarrow \text{B}}(t)$ is the time-of-flight for a signal that arrives at B at time t , as measured in oracle time. To solve these equations for the time offset between sites, $\Delta t_{\text{AB}} = \tau_{\text{A}} - \tau_{\text{B}}$, we need the integer values, p_{AX} , p_{BX} , and p_{XB} , as extracted from the communication-based O-TWTFT. We also need the time-of-flight non-reciprocity, Eq. (2), which is briefly derived here.

From (3) and the substitution mentioned afterwards, it is clear we are interested in the asymmetry $T_{\text{A} \rightarrow \text{B}}(f_r^{-1} k_{\text{pXB}} - \tau_{\text{B}}) - T_{\text{B} \rightarrow \text{A}}(f_r^{-1} k_{\text{pBX}} - \tau_{\text{A}})$. To first order in V/c ,

$$T_{\text{A} \rightarrow \text{B}}(f_r^{-1} k_{\text{pXB}} - \tau_{\text{B}}) = T_{\text{A} \rightarrow \text{B}}(f_r^{-1} k_{\text{pBX}} - \tau_{\text{A}}) + (V/c) [f_r^{-1} k_{\text{pXB}} - f_r^{-1} k_{\text{pBX}} + \Delta t_{\text{AB}}], \quad (4)$$

where the second term is the asynchronous sampling contribution. Because of the finite speed of light, $T_{\text{A} \rightarrow \text{B}}(f_r^{-1} k_{\text{pXB}} - \tau_{\text{B}}) \neq T_{\text{B} \rightarrow \text{A}}(f_r^{-1} k_{\text{pXB}} - \tau_{\text{B}})$. Instead, a simple geometric calculation gives

$T_{A \rightarrow B}(t) - T_{B \rightarrow A}(t) = (V/c)[L_A(t) - L_B(t)] + O((V/c)^2)$. Finally, we have the breakdown in reciprocity,

$$T_{A \rightarrow B}(f_r^{-1}k_{pXB} - \tau_B) - T_{B \rightarrow A}(f_r^{-1}k_{pBX} - \tau_A) = (V/c)[f_r^{-1}k_{pXB} - f_r^{-1}k_{pBX} + \Delta t_{AB}] + (V/c^2)[L_A - L_B] \quad (5)$$

for the time-of-flight of the remote and transfer comb pulses.

With this information, we can solve to find the time offset,

$$\Delta t_{AB} = \frac{1}{2 - V/c + \Delta f_r/f_r} \left\{ \frac{\Delta f_r}{f_r^2} \{2k_{pAX} - k_{pXB} - k_{pBX}\} + \frac{\Delta f_r}{f_r} T_{A \rightarrow B}(t_{pXB}) + f_r^{-1} [p_{XB} + p_{BX} - 2p_{AX}] + 2\Delta T_{cal} + \frac{V}{c} (f_r^{-1}k_{pXB} - f_r^{-1}k_{pBX} + c^{-1}[L_A - L_B] + 2\Delta T_{cal}^V) \right\} \quad (6)$$

where we introduce two calibration terms, ΔT_{cal} , ΔT_{cal}^V , discussed in the main text and Ref. 24, and drop terms of order $(V/c)^2$ and higher throughout. In the real-time computation, the closing velocity, V , is found by a combination of centered numerical derivatives using the previous three measurements of $T_{A \rightarrow B}$ and $T_{B \rightarrow A}$, which assumes constant acceleration over $3/\Delta f_r \sim 1.5$ ms.

The above derivation follows the general outline of previous quasi-static O-TWTFT algorithms and is intended to highlight some of the additional speed-dependent terms. However, in practice, the asynchronous sampling, ambiguity in the comb pulses, constantly changing time-of-flight, acceleration, and real-time processing constraints lead to a different implementation where the timing information from the communication-based TWTFT and comb-based timestamps are combined and interpolated to generate the effective four timestamps of Eq. (1). However, this treatment is more extensive and will be given in detail in Ref. 24.

Acknowledgements

This work was funded by the National Institute for Standards and Technology (NIST) and the Defense Advanced Research Projects Agency (DARPA) PULSE program. We thank Prem Kumar, Martha Bodine, Jennifer Ellis and Kyle Beloy for helpful discussions.

Author Contributions

HB, LCS, JDD, and NRN determined the effects of motion and designed the algorithms. HB, and JDD implemented the digital signal processing. HB, JDD, IK, LCS, and WCS acquired and analyzed the data. KCC designed and implemented the tracking terminal necessary for quadcopter operation. WCS designed and implemented the swept delay line. MC and KCC assisted with hardware implementation and quadcopter operation. LCS, JDD, and NRN prepared the manuscript.

Competing Interests

The authors declare no competing financial interests.

References

1. Cliche, J.-F. & Shillue, B. Precision timing control for radioastronomy: maintaining femtosecond synchronization in the Atacama Large Millimeter Array. *IEEE Control Syst.* **26**, 19–26 (2006).
2. Gill, P. When should we change the definition of the second? *Phil Trans R Soc A* **369**, 4109–4130 (2011).
3. Schiller, S. Feasibility of giant fiber-optic gyroscopes. *Phys. Rev. A* **87**, 033823 (2013).
4. Derevianko, A. & Pospelov, M. Hunting for topological dark matter with atomic clocks. *Nat. Phys.* **10**, 933–936 (2014).
5. Stadnik, Y. V. & Flambaum, V. V. Searching for Dark Matter and Variation of Fundamental Constants with Laser and Maser Interferometry. *Phys. Rev. Lett.* **114**, 161301 (2015).
6. Kolkowitz, S. *et al.* Gravitational wave detection with optical lattice atomic clocks. *Phys. Rev. D* **94**, 124043 (2016).
7. Takano, T. *et al.* Geopotential measurements with synchronously linked optical lattice clocks. *Nat. Photonics* **10**, 662–666 (2016).
8. Lisdat, C. *et al.* A clock network for geodesy and fundamental science. *Nat. Commun.* **7**, 12443 (2016).
9. Delva, P. *et al.* Test of Special Relativity Using a Fiber Network of Optical Clocks. *Phys. Rev. Lett.* **118**, 221102 (2017).
10. Grotti, J. *et al.* Geodesy and metrology with a transportable optical clock. *Nat. Phys.* **14**, 437–441 (2018).
11. Riehle, F. Optical clock networks. *Nat. Photonics* **11**, 25–31 (2017).
12. Mehlstäubler, T. E., Grosche, G., Lisdat, C., Schmidt, P. O. & Denker, H. Atomic clocks for geodesy. *Rep. Prog. Phys.* **81**, 064401 (2018).
13. Giorgetta, F. R. *et al.* Optical two-way time and frequency transfer over free space. *Nat. Photonics* **7**, 434–438 (2013).

14. Deschênes, J.-D. *et al.* Synchronization of Distant Optical Clocks at the Femtosecond Level. *Phys. Rev. X* **6**, 021016 (2016).
15. Bergeron, H. *et al.* Tight real-time synchronization of a microwave clock to an optical clock across a turbulent air path. *Optica* **3**, 441 (2016).
16. Sinclair, L. C. *et al.* Synchronization of clocks through 12 km of strongly turbulent air over a city. *Appl. Phys. Lett.* **109**, 151104 (2016).
17. Kirchner, D. Two-way time transfer via communication satellites. *Proc. IEEE* **79**, 983–990 (1991).
18. Fujieda, M. *et al.* Carrier-phase two-way satellite frequency transfer over a very long baseline. *Metrologia* **51**, 253 (2014).
19. Kim, J., Cox, J. A., Chen, J. & Kärtner, F. X. Drift-free femtosecond timing synchronization of remote optical and microwave sources. *Nat. Photon* **2**, 733–736 (2008).
20. Ning, B. *et al.* High-Precision Distribution of Highly Stable Optical Pulse Trains with 8.8×10^{-19} instability. *Sci. Rep.* **4**, (2014).
21. Krehlik, P., Śliwczyński, Ł., Buczek, Ł., Kołodziej, J. & Lipiński, M. Ultrastable long-distance fibre-optic time transfer: active compensation over a wide range of delays. *Metrologia* **52**, 82 (2015).
22. Bercy, A. *et al.* Two-way optical frequency comparisons at 5×10^{-21} relative stability over 100-km telecommunication network fibers. *Phys. Rev. A* **90**, 061802 (2014).
23. Calosso, C. E. *et al.* Frequency transfer via a two-way optical phase comparison on a multiplexed fiber network. *Opt. Lett.* **39**, 1177–1180 (2014).
24. Sinclair, L. C. *et al.* Femtosecond Optical Two-Way Time-Frequency Transfer in the Presence of Motion. Preprint at <https://arxiv.org/abs/1808.07040> (2018).
25. Ives, H. E. The Doppler Effect from Moving Mirrors. *JOSA* **30**, 255–257 (1940).
26. Isaac Khader *et al.* Time Synchronization over a Free-Space Optical Communication Channel. Preprint at <https://arxiv.org/abs/1808.06710> (2018).

27. Cossel, K. C. *et al.* Open-path dual-comb spectroscopy to an airborne retroreflector. *Optica* **4**, 724–728 (2017).
28. Robert, C., Conan, J.-M. & Wolf, P. Impact of turbulence on high-precision ground-satellite frequency transfer with two-way coherent optical links. *Phys. Rev. A* **93**, 033860 (2016).
29. Belmonte, A., Taylor, M. T., Hollberg, L. & Kahn, J. M. Effect of atmospheric anisoplanatism on earth-to-satellite time transfer over laser communication links. *Opt. Express* **25**, 15676–15686 (2017).
30. Richards, M. A. *Fundamentals of Radar Signal Processing, Second Edition*. (McGraw-Hill Education, 2014).

Figure Legends

Figure 1. (a) O-TWTFT to a quadcopter-mounted retroreflector. The light is polarization multiplexed between site A and site B and directed over the air to the quadcopter at up to 1 km distance. (b) O-TWTFT with a rapidly swept delay line and 0-4 km free-space path. In both configurations, co-location of sites A and B allows for out-of-loop synchronization verification. (c) Time deviation for synchronization over 4 km of air with the moving delay line at ± 24 m/s (blue circles) and for synchronization off of the quadcopter (green squares). (d) Still image from Supplementary Video 1 showing flight of the quadcopter looking back towards the tracking terminal and co-located clocks. (e) Still image from Supplementary Video 1 showing the calculated times (from system turn-on), the round trip propagation distance, the closing speed, and status.

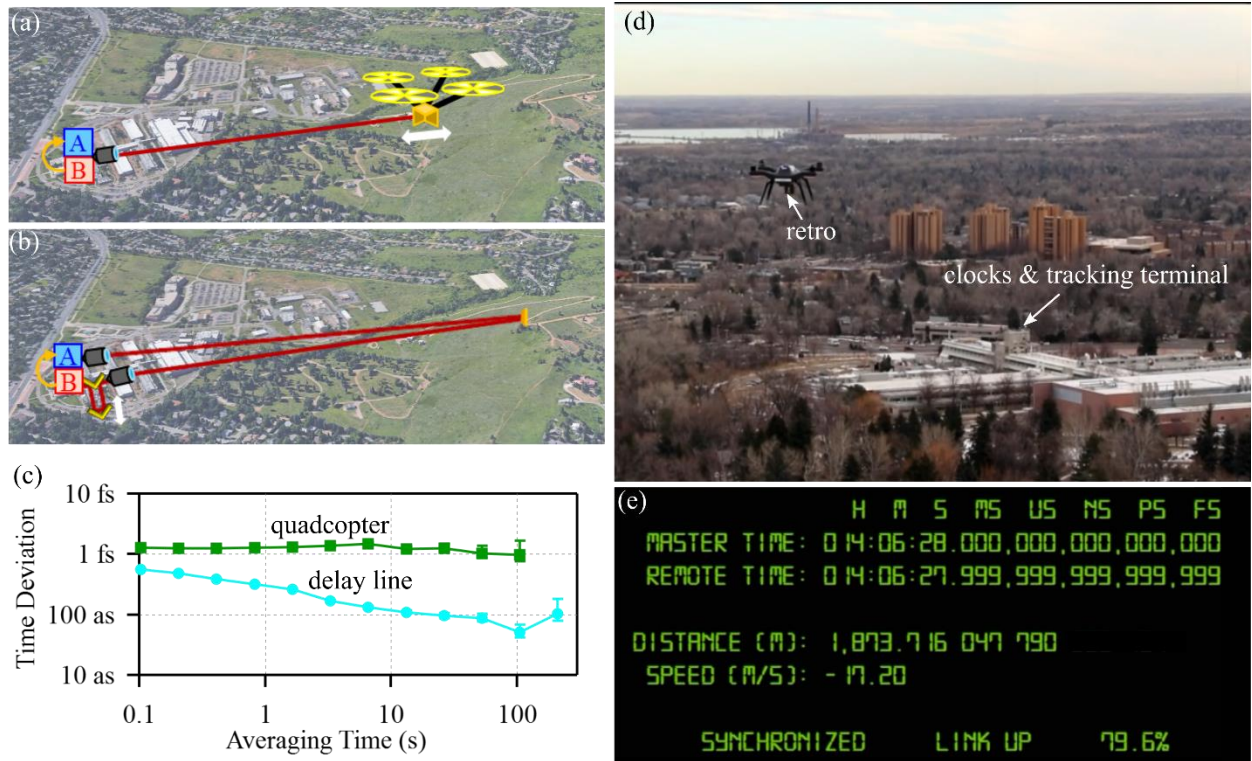
Figure 2: (a) Results from rapidly swept delay line operated at closing velocities ranging from 0 m/s to 24 m/s. The time-of-flight (top panel, left axis) and closing velocity (middle panel) are retrieved from the O-TWTFT data. The clock time offset (bottom panel) is the out-of-loop verification. During active synchronization (i.e. no long fades) the standard deviation is 1.1 fs. All data is at the 2.2 kHz update rate. (b) Expanded view. The clocks' time offset is shown for all time (cyan) and only during active synchronization, i.e. no turbulence-induced fades (black line).

Figure 3: (a) O-TWTFT to the quadcopter showing the pathlength (top panel), closing velocity (middle panel), and clocks' time offset (bottom panel), measured by the out-of-loop verification channel during periods of active synchronization. The standard deviation is 3.7 fs. All data is at the ~ 2 kHz update rate.

Figure 4: (a) Time deviation for O-TWTFT to the quadcopter with 0-20 m/s motion (open green squares) and for the swept delay line with ± 24 m/s motion and a free-space path length of 0 m (red

circles), 2 km (blue circles), and 4 km (cyan circles). Also shown is the time deviation at 0 m/s and 0 m free-space path (black circles). The elevated time deviation for the quadcopter data is due to longer signal dropouts and calibration uncertainties associated with the tracking terminal. The O-TWTFT synchronization bandwidth was 10 Hz. (b) Corresponding modified Allan deviation.

Figures



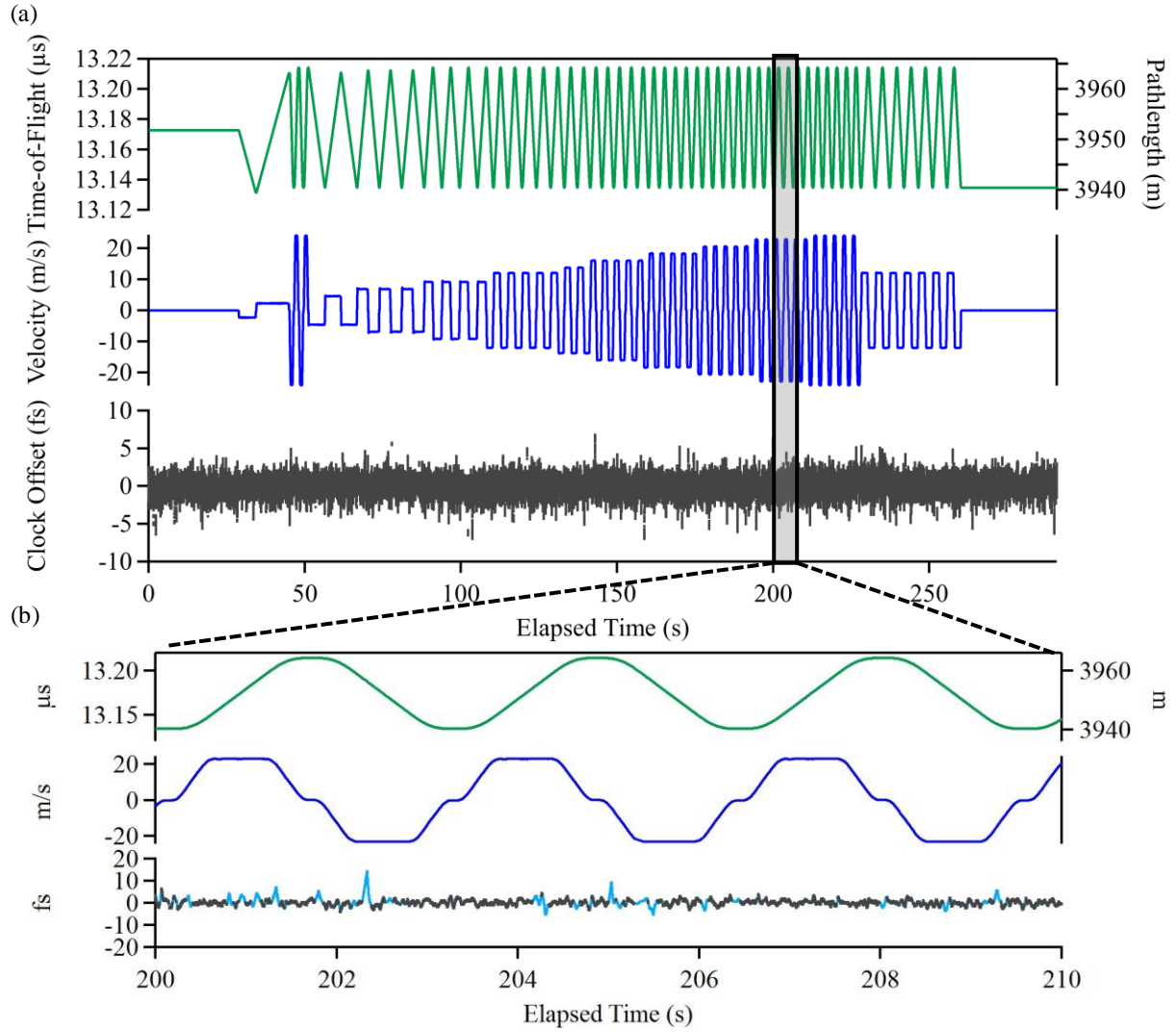


Figure 2: (a) Results from rapidly swept delay line operated at closing velocities ranging from 0 m/s to 24 m/s. The time-of-flight (top panel, left axis) and closing velocity (middle panel) are retrieved from the O-TWTFT data. The clock time offset (bottom panel) is the out-of-loop verification. During active synchronization (i.e. no long fades) the standard deviation is 1.1 fs. All data is at the 2.2 kHz update rate. (b) Expanded view. The clocks' time offset is shown for all time (cyan) and only during active synchronization, i.e. no turbulence-induced fades (black line).

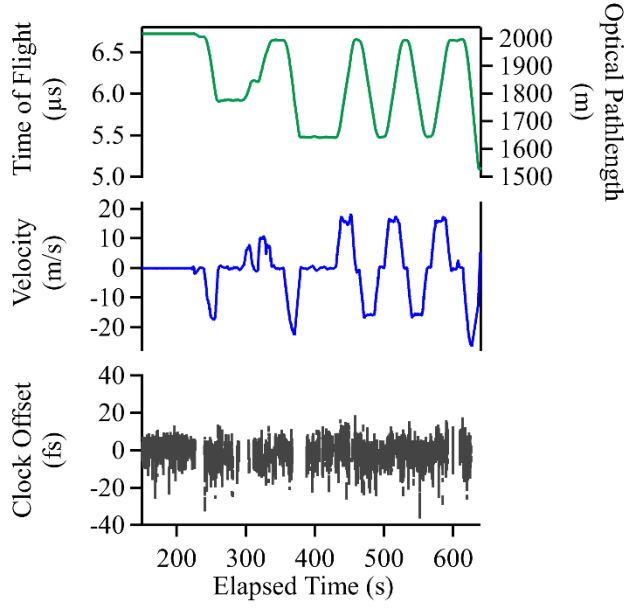


Figure 3: (a) O-TWTFT to the quadcopter showing the pathlength (top panel), closing velocity (middle panel), and clocks' time offset (bottom panel), measured by the out-of-loop verification channel during periods of active synchronization. The standard deviation is 3.7 fs at the ~ 2 kHz update rate.

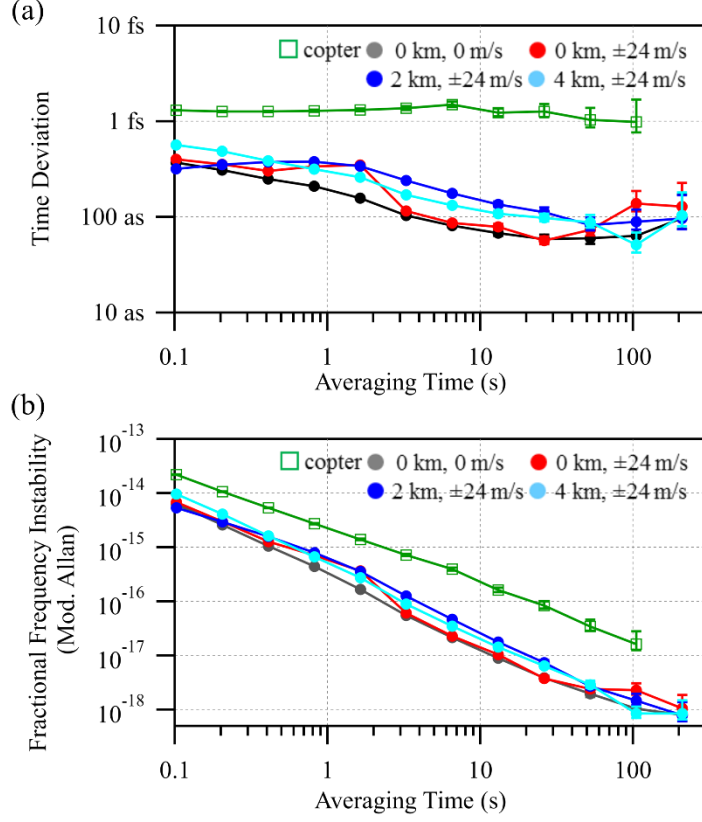


Figure 4: (a) Time deviation for O-TWTFT to the quadcopter with 0-20 m/s motion (open green squares) and for the swept delay line with ± 24 m/s motion and a free-space path length of 0 m (red circles), 2 km (blue circles), and 4 km (cyan circles). Also shown is the time deviation at 0 m/s and 0 m free-space path (black circles). The elevated time deviation for the quadcopter data is due to longer signal dropouts and calibration uncertainties associated with the tracking terminal. The O-TWTFT synchronization bandwidth was 10 Hz. (b) Corresponding modified Allan deviation.